PCCP

PAPER

View Article Online
View Journal | View Issue

Cite this: *Phys. Chem. Chem. Phys.*, 2019, **21**, 7781

Customizing topographical templates for aperiodic nanostructures of block copolymers *via* inverse design†

Runrong Zhang, Liangshun Zhang, * Jiaping Lin * and Shaoliang Lin

Received 5th February 2019,
Accepted 19th March 2019

DOI: 10.1039/c9cp00712a

rsc.li/pccp

The limited complexity of self-assembled nanostructures of block copolymers seriously impedes their potential utility in the semiconductor industry. Therefore, the customizability of complex nanostructures has been a long-standing goal for the utilization of directed self-assembly in nanolithography. Herein, we integrated an advanced inverse design algorithm with a well-developed theoretical model to deduce inverse solutions of topographical templates to direct the self-assembly of block copolymers into reproducible target structures. The deduced templates were optimized by finely tuning the input parameters of the inverse design algorithm and through symmetric operation as well as nanopost elimination. More importantly, our developed algorithm has the capability to search inverse solutions of topographical templates for aperiodic nanostructures over exceptionally large areas. These results reveal design rules for guiding templates for the device-oriented nanostructures of block copolymers with prospective applications in nanolithography.

Introduction

The directed self-assembly (DSA) of block copolymer thin films using chemical or topographical templates provides a promising opportunity to yield highly uniform, well registered, macroscopically ordered nanostructures with dimensions and periods at sub-10 nm scales.[1–9] These periodic nanostructures are employed as lithographic masks to fabricate a variety of nanodevices in the semiconductor industry, such as FinFETs, nanowire transistors or flash memory.[10–12] Nevertheless, the limited complexity of the DSA nanostructures of block copolymers seriously impedes prospective applications in nanofabrication. As a typical example, complex layouts encountered in logic devices still require aperiodic and discontinuous nanostructures.[13] This necessitates the customization of guiding templates at high resolution to program the formation of device-oriented nanostructures of block copolymers.

Most of the experimental and theoretical efforts to achieve the aperiodic nanostructures of block copolymers concentrate on the 'forward' problem, aimed at predicting possible nanostructures of block copolymers under specified geometries and chemical properties of templates such as the spacing and size of guiding motifs.[14–22] In other words, a given set of design parameters of templates are applied to scan over all possible nanostructures of block copolymers. For instance, using large-scale simulations of self-consistent field theory, we intuitively set up the topographical templates to generate simple aperiodic nanostructures of block copolymers including zigzag, T-junction and nested-elbow structures.[18,19] It should be noted that the forward approach to yielding the device-oriented nanostructures of block copolymers is strongly dependent upon the intuitive design of templates, where the arrangement of guiding motifs is similar to the topological features of nontrivial nanostructures. In addition, the forward approach has become challenging and expensive due to the scanning of an enormous design space of potential templates. These pose a significant stumbling block to rationally and precisely customizing the guiding templates for aperiodic nanostructures, which foreshadow the potential to fabricate multifunctional nanodevices.

A more pragmatic methodology is 'inverse' design: starting from an aperiodic (target) nanostructure, and searching for the optimum template that programs the formation of the desired nanostructure.[23–32] For example, Hannon *et al.* integrated a mean-field theory with a random search algorithm to seek inverse solutions of topographical templates for programming aperiodic T-junctions and discontinuous bends.[23,24] These studies provide a proof-of-principle demonstration of the inverse design algorithm for the intelligent construction of guiding templates. What is missing in Hannon's works is the

Shanghai Key Laboratory of Advanced Polymeric Materials, State Key Laboratory of Bioreactor Engineering, Key Laboratory for Ultrafine Materials of Ministry of Education, School of Materials Science and Engineering, East China University of Science and Technology, Shanghai, 200237, China. E-mail: zhangls@ecust.edu.cn, jlin@ecust.edu.cn

† Electronic supplementary information (ESI) available: Model and additional simulation results. See DOI: 10.1039/c9cp00712a

ability to customize topographical templates for nontrivial nanostructures over large areas, because the search algorithm rapidly becomes intractable under the circumstance of large-scale simulations.

In this contribution, on the basis of the hybrid particle-field model,[33,34] we improve the advanced inverse design method to customize topographical templates for reproducible structures of block copolymers. One key advantage of our improved method is its high efficiency in finding inverse solutions of topographical templates, in comparison with the conventional algorithm based on the random sampling of phase space. In addition, the inverse solutions can be further optimized by our improved method. Consequently, our method has the capability to search inverse solutions of topographical templates for complicated aperiodic nanostructures over exceptionally large areas, which cannot be achieved by other inverse design algorithms.

Theory and method

Self-consistent field theory (SCFT) is utilized to model the self-assembly of AB block copolymers directed by topographical templates with an array of nanoposts. Herein, the self-assembled nanostructures are represented by density fields ρ_I (I = A and B blocks). The nanoposts are described by 'cavity' functions varying from 1 at their center to 0 outside of the nanoposts.[33,34] Target structures are introduced by constrained fields *via* the Lagrange method.[35] As illustrated in Fig. S1 of the ESI,† three types of constrained fields are considered in the current work: T-junction structure (designated by T_1), nested-elbow structure (T_2) and large-area aperiodic structure (T_3), which contains a set of essential geometries for integrated circuit layouts.[14] It should be mentioned that the block copolymers cannot definitely self-assemble into these device-oriented nanostructures at specific locations without the guidance of templates.

We improved the inverse design algorithm originally proposed by Hannon *et al.* to customize the topographical templates of nanoposts for given target structures.[23,24] The outline for our inverse design algorithm is listed as follows:

(Step 1) An array of mobile nanoposts with number N_p and radius R_p are randomly placed into the target structures, which are enforced by the Lagrange method (eqn (S2) of ESI†).[35] As a typical example, the density fields for the target structure T_1 with T-junctions and isolated line are shown in Fig. 1a.

(Step 2) On the basis of the hybrid particle-field simulations,[33,34] the fields of polymer components and the positions of nanoposts are updated until the system reaches metastable configurations. The procedures can be listed as follows: (i) the self-consistent field equations for the polymer fluids are numerically solved in the real-space. (ii) The motion of nanoposts obeys Newton's motion equations $\mathbf{r}_j^{n+1} = \mathbf{r}_j^n + \mathbf{f}_j\Delta t + \theta_j$, where $\mathbf{r}_j^n$ is the center of the j-th nanopost at the n-th iteration, $\mathbf{f}_j$ is the total force acting on the j-th nanopost and θ_j is the Gaussian white noise. Note that the Lagrange fields are adjusted in the hybrid particle-field simulations. (iii) Step (i) is repeated until the mean-square displacement of nanoposts is less than $10^{-3}R_g^2$ (R_g is the ideal gyration radius of polymer chains) and the condition of $|1 - \rho_A - \rho_B - \rho_P| < 10^{-3}$ is satisfied. Such a configuration of nanoposts is considered as a candidate solution (Fig. 1b).

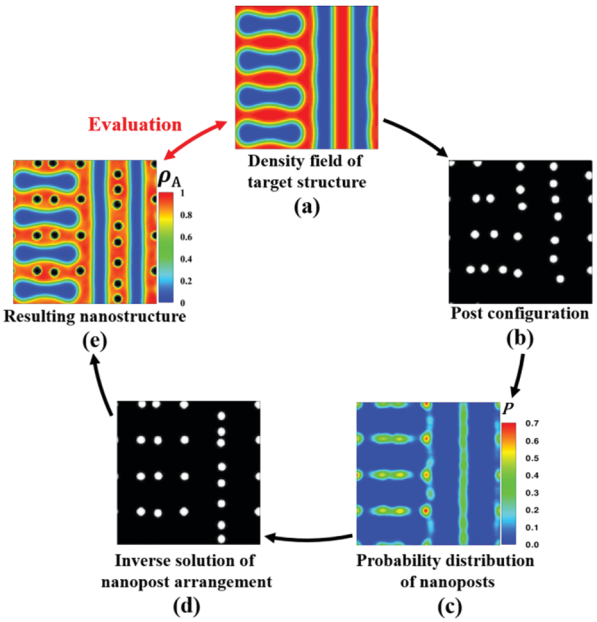

Fig. 1 A schematic illustration of the inverse design algorithm for target structure T_1. (a) Density fields of target structure obtained from Fig. S1 of ESI.† (b) The typical configuration of the nanopost array *via* the hybrid particle-field simulations. The white dots highlight the nanoposts. (c) The probability distribution of nanoposts by summing the nanopost position and normalization. (d) Deduced topographical template of the nanopost array considering the threshold setting of the probability distribution. (e) Density fields of the self-assembled nanostructure registered by the deduced template. The resulting nanostructure is compared with the target structure shown in panel (a).

(Step 3) The simulations are repeated under various initial configurations of mobile nanoposts and a statistical sampling probability distribution of nanoposts from all candidate solutions is obtained (Fig. 1c).

(Step 4) The topographical template with a specific number of immobile nanoposts is deduced through thresholding the probability distribution (p_{thresh}). The value of p_{thresh} is chosen such that the number of deduced nanoposts is close to the input value N_p of nanoposts in the 2nd step. Such an arrangement of nanoposts is considered to be an inverse solution, which is illustrated in Fig. 1d.

(Step 5) The deduced template is exploited to direct the self-assembly of block copolymers *via* forward SCFT simulations (*i.e.*, the constrained fields of target structures are released). The resulting self-assembled structure will be compared with the target structure (Fig. 1e). For more details about the inverse design algorithm, refer to Part A of the ESI.†

One important improvement of our proposed algorithm is that the hybrid particle-field simulations are utilized to generate metastable configurations of mobile nanoposts satisfying saddle point conditions of SCFT. Instead of the Monte Carlo

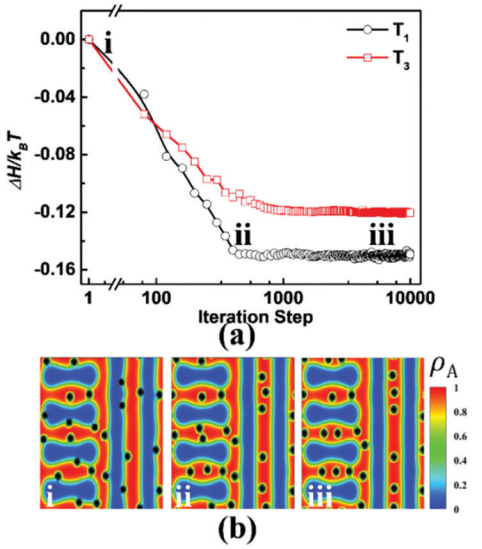

Fig. 2 (a) The free energy functional, $\Delta H/k_BT$, as a function of the iteration step of hybrid particle-field simulations during the implementation of the inverse design algorithm of topographical templates for target structures T_1 and T_3. (b) Typical configurations of mobile nanoposts in the presence of a constrained field of target structure T_1. The color bar shown in the right represents the strength of the density field of A blocks. The nanoposts are designated as the black dots. The labels of configurations match the Roman numbers in panel (a).

method updating the position of a single nanopost at each iteration, the scheme of Brownian motion is applied to move all the nanoposts at the same time. As a consequence, our improved algorithm of inverse design converges more quickly to the configuration with minimum energy, which is demonstrated in Fig. 2. Herein, the target structures T_1 and T_3 have sizes of $16R_g \times 16R_g$ and $72R_g \times 40R_g$, respectively. The numbers of mobile nanoposts are set as $N_p = 25$ and 200, respectively. The calculated results suggest that there exist two convergence rate regimes for the free energy functional as a function of the iteration step. In the range of #iteration < 500, the magnitude of the free energy functional has a sharp decrease (Fig. 2a), and the A-wetting nanoposts collectively move to the A-rich domains to depress the contribution of enthalpy (Fig. 2b and Fig. S2 of ESI†). Beyond the iteration step, the mobile nanoposts undergo random walk minimization in the A-rich domains to alleviate the contribution of conformational entropy, and the free energy functional displays a plateau. Fig. 2a also illustrates that the free energy functional reaches the plateau at #iteration $\approx$ 500, which is far less than the iteration steps reported by Hannon *et al.*[23] More importantly, such iteration steps are weakly dependent upon the number of mobile nanoposts and the size of target structures.

Results and discussion

We first demonstrated that inverse solutions of topographical templates can reproduce the target structures *via* tuning the input parameters of the improved algorithm (*i.e.*, number and radius of nanoposts). Fig. 3a shows the self-assembled structures registered by inverse solutions of topographical templates under various numbers N_p of nanoposts at fixed radius $R_p = 0.45R_g$. Because the mobile nanoposts do indeed move towards the T-shaped defects in the hybrid particle-field simulations (2nd step in the inverse design algorithm),[36,37] the probability distribution of nanoposts at the T-junctions has a high value. As a consequence, deduced templates consist of nanoposts at the T-junctions when N_p is small (cases of $N_p = 15$ and 20). However, the mobile nanoposts are randomly located at the isolated line, leading to a sparse arrangement of nanoposts at this region. Under these conditions, the topographical templates cannot guide the block copolymers to reproduce the target structures T_1. With an increase of N_p to 25, the inverse solution of topographical templates includes the nanoposts at both the T-junctions and the isolated line, which do indeed generate the density fields of A and B blocks close to those of target structure T_1.

Fig. 3b shows the effect of nanopost radius R_p on the inverse solutions of topographical templates and the corresponding self-assembled nanostructures of block copolymers. For the cases of $R_p = 0.30R_g$ and $0.50R_g$, arrangements of nanoposts in the deduced templates are similar. Since the registration ability for the case of $R_p = 0.30R_g$ is poor, the target structure is not reproduced by the directed self-assembly of block copolymers. The presence of large nanoposts (*e.g.*, $R_p = 0.50R_g$) greatly facilitates the formation of the target structure. However, the nanoposts with radius $R_p = 0.60R_g$ considerably distort polymer chains in the A-rich domains of the resulting nanostructure,[38] which does not match well with the target structure T_1.

In order to quantify the matching degree of the resulting structures registered by the inverse solutions, we introduced a

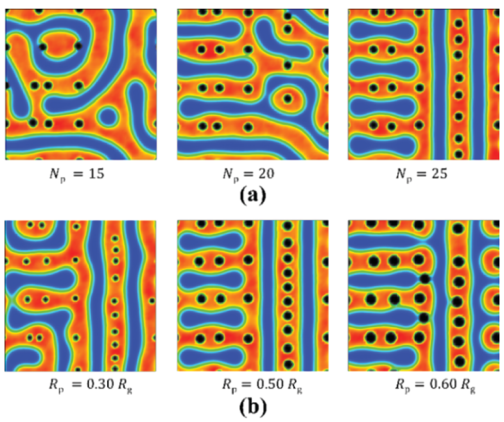

Fig. 3 Inverse solutions of topographical templates for target structure T_1 and the corresponding self-assembled nanostructures of block copolymers. (a) The effect of nanopost number N_p. The radius of the nanopost is fixed at $R_p = 0.45R_g$. (b) The effect of nanopost radius R_p. The number of nanoposts is fixed at $N_p = 25$. N_p and R_p are input parameters of hybrid particle-field simulations (2nd step in the inverse design algorithm). To maintain the approximate value of nanopost number N_p, various threshold values of probability distribution in the 4th step are chosen. The representations of colors are the same as those in Fig. 2b.

fidelity parameter to evaluate the difference between the target and resulting structures. As illustrated in Fig. S3 of ESI,† the skeletonization algorithm is used to identify the topology and connectivity of lamellar domains represented by skeleton lines.[39] The fidelity parameter ξ is defined as

$$\xi = \frac{N_{M_T(\mathbf{r})=1} - N_{\Omega(\mathbf{r})=1}}{N_{M_T(\mathbf{r})=1}}$$

where $N_{M_T(\mathbf{r})=1}$ represents the total point number of skeleton lines of the target structure and $N_{\Omega(\mathbf{r})=1}$ corresponds to the number of incorrect/missing points of the resulting structures. As the fidelity parameter ξ becomes large, the matching degree of resulting structures is boosted. When the fidelity parameter is larger than the critical value $\xi_c = 0.98$, inverse solutions of topographical templates have the capability to reproduce the target structure. It should be pointed out that the fidelity parameter ξ could be negative if the topographical templates are inefficient.

Fig. 4a shows the fidelity parameter in terms of the number and radius of nanoposts. The dashed line highlights the critical value of the fidelity parameter. As shown in Fig. 4a, small values of nanopost number produce poor solutions of topographic templates. Above a critical value of N_p, the deduced templates successfully direct the block copolymers to self-assemble into the target structure. To minimize the fabrication time of the topographical template in the experiments of nanolithography, it is desirable for the nanoposts to be as sparse as possible (*i.e.*, the critical value of nanopost number is the optimum solution of topographical templates, which is designated as N_p^{opt}). However, the effect of the nanopost radius displays a different behavior (inset of Fig. 4a). If the value of R_p is too small or too large, the resulting structures with features of missing or extra connections are produced, and the inverse solutions of topographical templates are rejected according to the topology and connectivity criterions of the target structure. The large value of the fidelity parameter in the range of $0.45R_g \leq R_p \leq 0.55R_g$ indicates the best solution of topographical templates for the case of $N_p = 25$, where the resulting structures match well with the target structure.

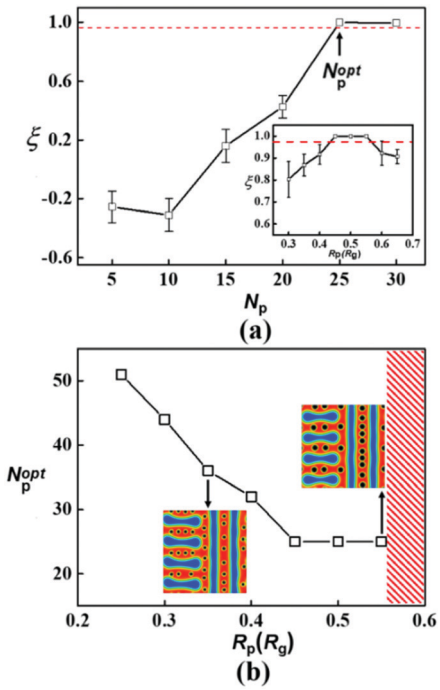

Fig. 4 (a) Fidelity parameter ξ in terms of the number N_p of nanoposts and the radius R_p of nanoposts (inset). The dashed line highlights the critical value ξ_c of the fidelity parameter. Each data point is collected from ten independent runs of forward SCFT simulations using different initial configurations for the given inverse solution of the topographical template, and the error bars represent the standard deviations. (b) The optimum number of nanoposts as a function of the radius R_p of nanoposts. Insets show the self-assembled nanostructures programmed by inverse solutions of topographical templates for the cases of $R_p = 0.35R_g$ and $0.55R_g$. The shaded area indicates the case of $R_p > 0.55R_g$.

Furthermore, we probed into the effect of the nanopost radius R_p on the optimum number N_p^{opt} of nanoposts needed to achieve the reproduction of the target structure T_1, which is summarized in Fig. 4b. Note that the radius of nanoposts should be larger than the grid size of the simulation boxes (*i.e.*, $R_p \geq 0.25R_g$). The nanoposts with radius $R_p > 0.55R_g$ distort the lamellar domains of the block copolymers and are not considered in the inverse design algorithm of topographical templates (shaded area in Fig. 4b). It is found from Fig. 4b that the optimum number N_p^{opt} of nanoposts is strongly dependent upon the radius of the nanoposts. Specifically, when the nanopost radius is small (*e.g.*, $0.25R_g \leq R_p \leq 0.45R_g$), lots of nanoposts in the inverse solutions of topographical templates are required to facilitate the reproduction of the target structure T_1. In the range of $0.45R_g \leq R_p \leq 0.55R_g$, the optimum number N_p^{opt} of nanoposts maintains the value of ~ 25. The phenomena indicate that the optimum number ($N_p \approx 25$) and radius ($0.45R_g \leq R_p \leq 0.55R_g$) of the mobile nanoposts can be used to deduce the effective templates for the target structure T_1.

The inverse solutions of topographical templates are also affected by the selectivity of the nanoposts. Similar to the case of the A-wetting nanoposts, topographical templates consisting of an array of B-wetting nanoposts were deduced and are shown in Fig. S4 of the ESI.† The arrangement of B-wetting nanoposts is different from the case of A-wetting nanoposts (Fig. 3 and insets of Fig. S4 of the ESI†). However, the effects of the input parameters of the inverse design algorithm on the fidelity parameter have similar behaviors. In particular, there are given parameters of number and radius of the nanoposts to yield the effective templates (Fig. 4a and Fig. S4 of ESI†).

The inverse design of topographical templates for the device-oriented nanostructures has been reported in the simulation studies of Hannon and co-workers,[23,24] where a Monte-Carlo-like search algorithm is used to determine the arrangement of nanoposts. In these studies, the number and radius of nanoposts are varied to optimize the inverse solutions of topographical templates. Through evaluating the topology and connectivity of resulting structures, it was demonstrated that the quality of inverse solutions became better as the nanopost number of the inverse design algorithm increased (Fig. 3 in ref. 24). As shown in Fig. 3 and 4, the general tendencies of inverse solutions in terms

of the number of nanoposts are reasonably reproduced by the integration of the inverse design method with hybrid particle-field simulations. Therefore, the comparisons verify the validity of our improved algorithm for the inverse solutions of topographical templates.

Despite the identical tendencies of topographical templates in terms of the input parameters of the inverse design algorithm, there exists a difference in the arrangement of the nanoposts. In Hannon's studies, it was reported that the nanoposts were not necessarily located at the cores of lamellar defects such as bends or T-junctions. In our work, taking advantage of the high efficiency of the improved algorithm, we performed a series of simulations to search the inverse solutions of topographical templates with various nanopost radii. It was found that the small nanoposts (*e.g.*, $R_p = 0.35R_g$ in the inset of Fig. 4b) are not located at the centers of junctions. This arrangement of nanoposts in the topographical templates is similar to the finding of Hannon and co-workers. However, the nanoposts with larger radius have a strong tendency to emerge at the defects' cores in order to relieve the stretching of polymer chains (Fig. 3 and 4).[36,37] To the best of our knowledge, this is the first example clarifying the effect of the nanoparticle radius of the inverse design algorithm on the inverse solutions of topographical templates. Such a finding provides a useful guideline for experimentalists to rationally design the topographical templates for the achievement of aperiodic nanostructures with promising applications in the field of integrated circuit layouts.

To demonstrate the necessary condition of our deduced templates consisting of an array of nanoposts with larger radii, several simulations were performed for the self-assembly of block copolymers guided by the modified inverse solutions, where one of the nanoposts at the T-junction was removed. As shown in Fig. S5a of ESI,† the modified template cannot guide the block copolymers to self-assemble into the target structure. The computational results demonstrate the necessary condition of topographical templates consisting of nanoposts at the T-junctions.

It is worth pointing out that the existence of isolated lines in the target structure T_1 facilitates the formation of T-junctions. When the nanoposts programming the formation of isolated lines are removed, the modified templates direct the block copolymers to form perfect lamellae (Fig. S5b of ESI†). As comparisons, we also deduced inverse solutions of topographical templates for target structures consisting only of T-junctions (Fig. 5a). Under the conditions of $N_p = 25$ and $R_p = 0.45R_g$ (the same parameter settings of Fig. 3a), the inverse solution of the topographical template cannot reproduce the target structure (Fig. 5b). As the values of N_p and R_p are increased, deduced templates consist of the nanoposts both at the cores of T-junctions and the interspace of adjoining junctions, which synergistically direct the block copolymers to form the T-junctions at specific locations (Fig. 5c and d). These phenomena manifest the fact that an array of nanoposts with stronger registration ability is necessary for topographical templates to yield the T-junctions without the help of the isolated line. Note that such topographical templates with removed nanoposts cannot guide the block copolymers to self-assemble into the target structure (Fig. S6 of ESI†).

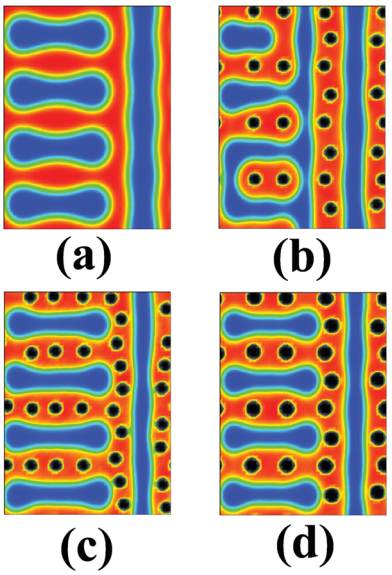

Fig. 5 (a) Target structure containing only an array of T-junctions. (b–d) Inverse solutions of topographical templates and the corresponding self-assembled nanostructures of block copolymers under the conditions of (b) $N_p = 25$ and $R_p = 0.45R_g$, (c) $N_p = 30$ and $R_p = 0.45R_g$ and (d) $N_p = 25$ and $R_p = 0.55R_g$.

Next, we utilized the improved algorithm to deduce topographical templates for the highly symmetric nested-elbow structure T_2, which contains lots of sharp bends and straight lines (Fig. S1b of ESI†). The size of the simulation boxes was set as $32R_g \times 32R_g$. Fig. 6a illustrates a representative solution of a topographical template for the target structure T_2. Due to the existence of straight lines in the target structure, the mobile nanoposts are randomly located at these regions during hybrid particle-field simulations, resulting in a dense arrangement of nanoposts in the deduced templates. In order to yield a sparse arrangement of nanoposts, we proceeded to further optimize the inverse design algorithm. Considering the high symmetry of the target structure, the probability distribution of nanoposts in the 3rd step of the inverse design algorithm was averaged by symmetric operation (Fig. 6b). In the 4th step, when multiple nanoposts in the regions of straight lines are near each other, one or more nanoposts are removed and then any remaining nanoposts are moved to the middle of the two nearest nanoposts (Fig. 6c). Fig. 6d shows the optimized arrangement of nanoposts and the corresponding self-assembled structure of block copolymers. The number of nanoposts in the inverse solution is reduced from 110 to 92 through the symmetric operation of probability distribution and the elimination of nanoposts. The topographical template with the optimized arrangement of nanoposts could direct the block copolymers to self-assemble into the target structure T_2.

Fig. 7 presents the effects of the number and radius of nanoposts on the inverse solutions of topographical templates for target structure T_2 and the corresponding registered

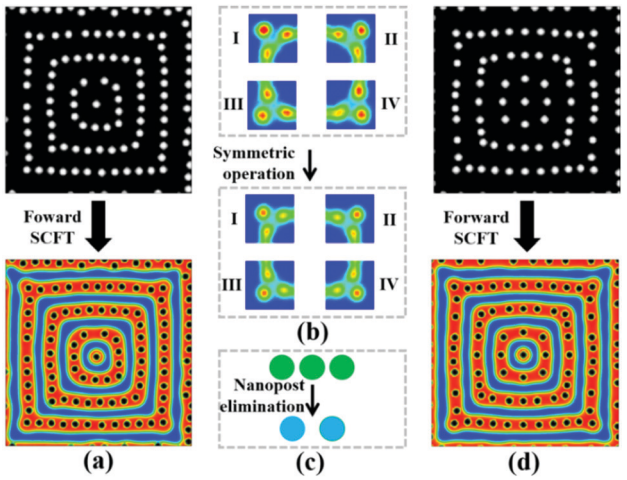

Fig. 6 (a) Upper panel: Inverse solution of the topographical template for target structure T_2. Bottom panel: Self-assembled nanostructure of block copolymers registered by the inverse solution. (b) Schematic illustration of the symmetric operation for the probability distribution of nanoposts. Only a portion of the probability distribution labeled by Roman numbers is shown and the corresponding overall view is shown in Fig. S7 of the ESI.† (c) Schematic illustration of the elimination of closely spaced nanoposts. (d) Upper panel: Optimized arrangement of nanoposts through symmetric operation and nanopost elimination; bottom panel: self-assembled nanostructure of block copolymers registered by the optimized template.

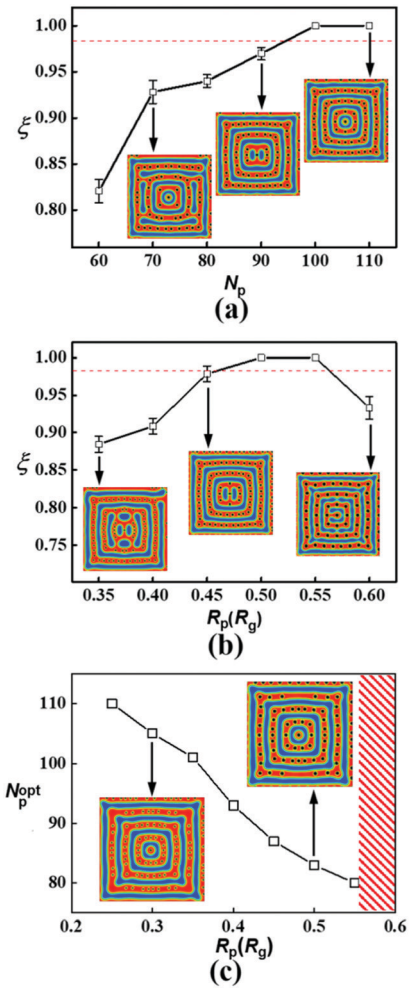

Fig. 7 (a) The fidelity parameter ξ as a function of the number N_p of nanoposts for the target structure T_2. The radius of nanoposts is fixed at $R_p = 0.50R_g$. (b) The fidelity parameter ξ as a function of the radius R_p of nanoposts. The number of nanoposts is fixed at $N_p = 110$. (c) The optimum number of nanoposts as a function of the radius R_p of nanoposts. Insets are the resulting structures directed by the topographical templates, which are optimized through the symmetric operation of probability distribution and the elimination of closely spaced nanoposts.

nanostructures of block copolymers. The fidelity parameter displays a monotonic behavior in terms of the nanopost number (Fig. 7a). However, the fidelity parameter as a function of the nanopost radius shows a non-monotonic behavior (Fig. 7b). The optimum number N_p^{opt} of nanoposts has a tight relationship with the radius of nanoposts (Fig. 7c). The predicted results are generally consistent with the findings shown in Fig. 3 and 4 for the case of target structure T_1.

With these backgrounds in place, we finally shifted our focus to a more challenging issue, demonstrating the feasibility of the inverse design of topographical templates over a large area. Herein, we chose the target structure T_3 with dense sharp bends, T-junctions and straight lines (Fig. S1c of ESI†), which has a size of $72R_g \times 40R_g$. The number and radius of nanoposts are set as $N_p = 320$ and $R_p = 0.55R_g$, respectively. Through the symmetric operation and nanopost elimination mentioned above, the optimized template consists of 273 nanoposts, which are represented by the black dots in Fig. 8. With the help of a guiding template, the block copolymers self-assemble into the nontrivial structure with bends, T-junctions and straight lines at specific locations, which is extremely similar to the target structure T_3 in the topology and connectivity. Through the skeletonization analysis, it was further confirmed that the resulting structure matches well with the target structure. Therefore, the inverse solution of the topographical template deduced from our improved algorithm has the capability to reproduce the target structure over an exceptionally large area.

As illustrated above, our improved algorithm for the inverse solutions of topographical templates provides advantages in the context of performance. First of all, instead of a Monte-Carlo-like search algorithm, the hybrid particle-field simulations are utilized to seek the arrangement of nanoposts, resulting in high computational efficiency to yield the inverse solutions of topographical templates (Fig. 2). Second, the optimum number of nanoposts needed to achieve the reproduction of the target structure is obtained (Fig. 4 and 7). Furthermore, considering the symmetry of target structures and the arrangement of closely spaced nanoposts, the deduced templates can be optimized through symmetric operation and the nanopost elimination (Fig. 6). These optimization processes in the inverse design algorithm will dramatically shorten the electron-beam writing times and lower fabrication cost of semiconductor devices. Third, due to the incorporation of hybrid particle-field simulations, the improved algorithm of inverse design could be applied to customize the topographical templates for aperiodic nanostructures over

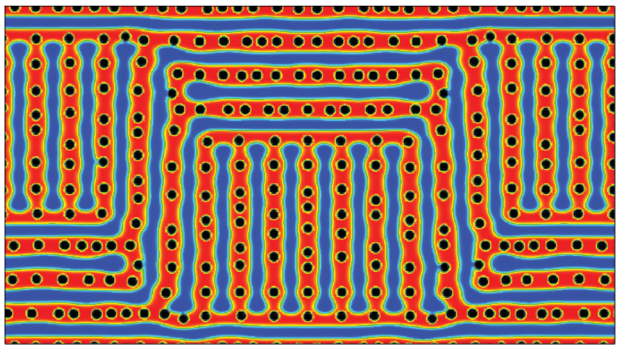

Fig. 8 Inverse solution of topographical template for target structure T_3 and corresponding self-assembled nanostructure of block copolymers. The input parameters of the inverse design algorithm are chosen as $N_p = 320$ and $R_p = 0.55R_g$. The inverse solution is optimized by symmetric operation and nanopost elimination.

exceptionally large areas (Fig. 8), which cannot be achieved by other inverse algorithms. Consequently, our proposed algorithm provides significant advancement to engineer the topographical templates with complicated layouts of nanoposts for the directed self-assembly of block copolymers.

Although our proposed algorithm presented here provides a highly efficient method for deducing the inverse solutions of topographical templates, there are still a few limitations in the cases of the directed self-assembly of block copolymers. First of all, our SCF calculations are performed in a two-dimensional (2D) cell because the three-dimensional (3D) calculations require a considerable amount of computational costs and the inverse design algorithm requires a large number of samples from independent simulations. It has been reported that the 3D nanostructures of block copolymers can be manipulated by modulating the design parameters of guiding templates.[40–42] Under these conditions, the height characteristic of nanoposts should be considered in the model of 3D nanostructures.[19] However, considering the potential applications of block copolymers as nanolithographic masks, our current work only involves the case of thin films with a thickness comparable to the ideal gyration radius of polymer chains, which are usually investigated by the 2D model.[43,44] The 2D calculations are able to capture the general features of nanostructures registered by the nanoposts. It is worth emphasizing that the height of nanoposts in the topographical templates is about half of block copolymer thin films in the experimental realizations of directed self-assembly for the applications of nanolithographic masks.[16,18]

Secondly, the target structures considered in this work are metastable patterns with grain boundaries between coexisting domains. We also apply our improved algorithm to deduce the inverse solutions of topographical templates for arbitrary target patterns (*e.g.*, M-like target nanostructure without grain boundaries). As shown in Fig. S8 of ESI,† our proposed algorithm of inverse design has the capability to customize the topographical templates for arbitrary target patterns. Herein, sparked by the idea of the designability of protein,[45] we introduced the parameter D to describe "designability" on the basis of the stability of the target structure. The parameter D is defined as the ratio of the area (S) of the target nanostructure to the total perimeter ($2\pi R_p N_p^{opt}$) of nanoposts, *i.e.*, $D \equiv S/2\pi R_p N_p^{opt}$, where N_p^{opt} is the optimum number of nanoposts with radius R_p as shown in Fig. 4 and 7. As the ratio D is increased, the target structure becomes easily stabilized and has a good "designability". For the target structures T_1, T_2, T_3 and the M-like structure, the average ratios D have the values of $3.26R_g$, $4.48R_g$, $3.05R_g$ and $2.20R_g$, respectively. Thus, the M-like target structure has a poor "designability" for the inverse solutions of topographical templates.

Conclusions

We have demonstrated the high efficiency of an improved algorithm for inversely designing the topographical templates with an array of nanoposts, which were exploited to direct the self-assembly of block copolymers into reproducible target structures with aperiodic characteristics. The inverse solutions of topographical templates can be finely tuned by the input parameters of the improved algorithm, and further optimized through the symmetric operation as well as the nanopost elimination. More importantly, our improved algorithm is able to seek the inverse solutions of topographical templates for the aperiodic structures over large area. The preceding results could provide useful information to rationally customize the topographical template for programming the formation of aperiodic nanostructures of block copolymers.

Conflicts of interest

There are no conflicts to declare.

Acknowledgements

This work was supported by the National Natural Science Foundation of China (21574040, 21873029 and 51833003).

References

1 R. A. Segalman, *Mater. Sci. Eng., R*, 2005, **48**, 191–226.
2 M. P. Stoykovich, M. Müller, S. O. Kim, H. H. Solak, E. W. Edwards, J. J. de Pablo and P. F. Nealey, *Science*, 2005, **308**, 1442–1446.
3 R. Ruiz, H. Kang, F. A. Detcheverry, E. Dobisz, D. S. Kercher, T. R. Albrecht, J. J. de Pablo and P. F. Nealey, *Science*, 2008, **321**, 936–939.
4 I. Bita, J. K. W. Yang, Y. S. Jung, C. A. Ross, E. L. Thomas and K. K. Berggren, *Science*, 2008, **321**, 939–943.
5 M. Luo and T. H. Epps III, *Macromolecules*, 2013, **46**, 7567–7579.
6 H. S. Suh, D. H. Kim, P. Moni, S. Xiong, L. E. Ocola, N. J. Zaluzec, K. K. Gleason and P. F. Nealey, *Nat. Nanotechnol.*, 2017, **12**, 575–581.
7 J. Zhang, M. B. Clark, C. Wu, M. Li, P. Trefonas III and P. D. Hustad, *Nano Lett.*, 2016, **16**, 728–735.

8 X. Man, D. Andelman and H. Orland, *Macromolecules*, 2010, **43**, 7261–7268.
9 X. Man, D. Andelman and H. Orland, *Phys. Rev. E: Stat., Nonlinear, Soft Matter Phys.*, 2012, **86**, 010801.
10 O. Hellwig, J. K. Bosworth, E. Dobisz, D. Kercher, T. Hauet, G. Zeltzer, J. D. Risner-Jamtgaard, D. Yaney and R. Ruiz, *Appl. Phys. Lett.*, 2010, **96**, 052511.
11 C. T. Black, *Appl. Phys. Lett.*, 2005, **87**, 163116.
12 H. Tsai, J. W. Pitera, H. Miyazoe, S. Bangsaruntip, S. U. Engelmann, C.-C. Liu, J. Y. Cheng, J. J. Bucchignano, D. P. Klaus, E. A. Joseph, D. P. Sanders, M. E. Colburn and M. A. Guillorn, *ACS Nano*, 2014, **8**, 5227–5232.
13 D. J. C. Herr, *J. Mater. Res.*, 2011, **26**, 122–139.
14 M. P. Stoykovich, H. Kang, K. C. Daoulas, G. Liu, C.-C. Liu, J. J. de Pablo, M. Müeller and P. F. Nealey, *ACS Nano*, 2007, **1**, 168–175.
15 G. Liu, C. S. Thomas, G. S. W. Craig and P. F. Nealey, *Adv. Funct. Mater.*, 2010, **20**, 1251–1257.
16 J. K. W. Yang, Y. S. Jung, J.-B. Chang, R. Mickiewicz, A. Alexander-Katz, C. Ross and K. K. Berggren, *Nat. Nanotechnol.*, 2010, **5**, 256–260.
17 H. Yi, X.-Y. Bao, R. Tiberio and H. S. P. Wong, *Nano Lett.*, 2015, **15**, 805–812.
18 L. Zhang, L. Wang and J. Lin, *ACS Macro Lett.*, 2014, **3**, 712–716.
19 X. Cao, L. Zhang, J. Gu, L. Wang and J. Lin, *Polymer*, 2015, **72**, 10–20.
20 G. S. Doerk, J. Y. Cheng, G. Singh, C. T. Rettner, J. W. Pitera, S. Balakrishnan, N. Arellano and D. P. Sanders, *Nat. Commun.*, 2014, **5**, 5805.
21 X. Man, J. Tang, P. Zhou, D. Yan and D. Andelman, *Macromolecules*, 2015, **48**, 7689–7697.
22 X. Man, P. Zhou, J. Tang, D. Yan and D. Andelman, *Macromolecules*, 2016, **49**, 8241–8248.
23 A. F. Hannon, K. W. Gotrik, C. A. Ross and A. Alexander-Katz, *ACS Macro Lett.*, 2013, **2**, 251–255.
24 A. F. Hannon, Y. Ding, W. Bai, C. A. Ross and A. Alexander-Katz, *Nano Lett.*, 2014, **14**, 318–325.
25 J. B. Chang, H. K. Choi, A. F. Hannon, A. Alexander-Katz, C. A. Ross and K. K. Berggren, *Nat. Commun.*, 2014, **5**, 3305.
26 K. R. Gadelrab, A. F. Hannon, C. A. Ross and A. Alexander-Katz, *Mol. Syst. Des. Eng.*, 2017, **2**, 539–548.
27 J. Qin, G. S. Khaira, Y. Su, G. P. Garner, M. Miskin, H. M. Jaeger and J. J. de Pablo, *Soft Matter*, 2013, **9**, 11467–11472.
28 G. S. Khaira, J. Qin, G. P. Garner, S. Xiong, L. Wan, R. Ruiz, H. M. Jaeger, P. F. Nealey and J. J. de Pablo, *ACS Macro Lett.*, 2014, **3**, 747–752.
29 M. Z. Miskin, G. Khaira, J. J. de Pablo and H. M. Jaeger, *Proc. Natl. Acad. Sci. U. S. A.*, 2016, **113**, 34–39.
30 B. A. Lindquist, R. B. Jadrich and T. M. Truskett, *J. Chem. Phys.*, 2016, **145**, 111101.
31 S. P. Paradiso, K. T. Delaney and G. H. Fredrickson, *ACS Macro Lett.*, 2016, **5**, 972–976.
32 M. R. Khadilkar, S. Paradiso, K. T. Delaney and G. H. Fredrickson, *Macromolecules*, 2017, **50**, 6702–6709.
33 S. W. Sides, B. J. Kim, E. J. Kramer and G. H. Fredrickson, *Phys. Rev. Lett.*, 2006, **96**, 250601.
34 Q. Zhang, L. Zhang and J. Lin, *J. Phys. Chem. C*, 2017, **121**, 23705–23715.
35 K. S. Lyakhova, A. V. Zvelindovsky, G. J. A. Sevink and J. G. E. M. Fraaije, *J. Chem. Phys.*, 2003, **118**, 8456–8459.
36 Y. Kim, H. Chen and A. Alexander-Katz, *Soft Matter*, 2014, **10**, 3284–3291.
37 J. Koski, B. Hagberg and R. A. Riggleman, *Macromol. Chem. Phys.*, 2016, **217**, 509–518.
38 J.-B. Chang, J. G. Son, A. F. Hannon, A. Alexander-Katz, C. A. Ross and K. K. Berggren, *ACS Nano*, 2012, **6**, 2071–2077.
39 T. Y. Zhang and C. Y. Suen, *Commun. ACM*, 1984, **27**, 236–239.
40 K. G. Tavakkoli, K. W. Gotrik, A. F. Hannon, A. Alexander-Katz, C. A. Ross and K. K. Berggren, *Science*, 2012, **336**, 1294–1298.
41 K. C. Daoulas, M. Müller, M. P. Stoykovich, S. M. Park, Y. J. Papakonstantopoulos, J. J. de Pablo, P. F. Nealey and H. H. Solak, *Phys. Rev. Lett.*, 2006, **96**, 036104.
42 M. Müller, *Phys. Rev. Lett.*, 2012, **108**, 087801.
43 P. Tang, F. Qiu, H. Zhang and Y. Yang, *Phys. Rev. E: Stat., Nonlinear, Soft Matter Phys.*, 2004, **69**, 031803.
44 A. Mickiewicz, J. K. W. Yang, A. F. Hannon, Y. Jung, A. Alexander-Katz, K. K. Berggren and C. A. Ross, *Macromolecules*, 2010, **43**, 8290–8295.
45 H. Li, R. Helling, C. Tang and N. Wingreen, *Science*, 1996, **273**, 666–669.

